THE ASTROPHYSICAL JOURNAL, 522:338–348, 1999 September 1
© 1999. The American Astronomical Society. All rights reserved. Printed in U.S.A.

OBSERVATIONS OF H_3^+ IN DENSE MOLECULAR CLOUDS

B. J. MCCALL
Department of Astronomy and Astrophysics, Department of Chemistry, and the Enrico Fermi Institute, University of Chicago, Chicago, IL 60637; bjmccall@uchicago.edu
T. R. GEBALLE[1]
Joint Astronomy Centre, Hilo, HI 96720
K. H. HINKLE
National Optical Astronomy Observatories,[2] Tucson, AZ 85726
AND
T. OKA
Department of Astronomy and Astrophysics, Department of Chemistry, and the Enrico Fermi Institute, University of Chicago, Chicago, IL 60637
Received 1998 December 21; accepted 1999 April 13

ABSTRACT

H_3^+ has been detected using infrared absorption spectroscopy along the lines of sight to six infrared sources in dense molecular clouds: AFGL 2136, W33A, Mon R2 IRS 3, AFGL 961E, AFGL 2591, and AFGL 490. Upper limits to the column densities of H_3^+ are reported for an additional nine sources. The column densities of CO toward Mon R2 IRS 3 and AFGL 961E have been determined from observations of the first-overtone lines of CO. For the six sources toward which H_3^+ was detected, a simple model of H_3^+ chemistry has been used together with column densities of H_2 derived from infrared CO measurements to estimate column lengths, mean number densities, and temperatures of molecular clouds. The derived column lengths are on the order of a parsec, the number densities are 10^4–10^5 cm^{-3}, and the temperatures are $\sim$25–50 K.

Subject headings: infrared: ISM: lines and bands — ISM: clouds — ISM: molecules — molecular processes

1. INTRODUCTION

The H_3^+ molecular ion plays the pivotal role in the gas-phase chemistry of the interstellar medium, as it initiates a chain of ion-neutral reactions that produce many of the chemical species detected by radio and infrared astronomers (Herbst & Klemperer 1973; Watson 1973). H_3^+ does not have a well-bound electronic excited state and therefore does not have a sharp electronic spectrum. Also, the symmetry of the equilateral triangle configuration of H_3^+ forbids a conventional rotational spectrum. Consequently, the detection of this important ion in the interstellar medium was not possible until the infrared spectrum was measured in the laboratory (Oka 1980) and until high-resolution array spectrometers enabled high-sensitivity spectroscopy in the infrared.

The first detection of H_3^+ in the interstellar medium came in 1996 in dense molecular clouds along the line of sight to the embedded young stellar objects AFGL 2136 and W33A (Geballe & Oka 1996). Subsequently, H_3^+ has been detected in the diffuse interstellar medium toward the visible star Cygnus OB2 No. 12 and toward two Galactic center sources whose lines of sight include both diffuse and dense clouds (McCall et al. 1998a; Geballe et al. 1999).

The H_3^+ ion serves as an important probe of molecular clouds because of a unique feature of its chemistry—the number density of H_3^+ is approximately independent of the total number density in the dense cloud environment. A simple model of H_3^+ formation and destruction can be used to estimate its number density, and the observed column density then provides an estimate of the effective path length through the cloud. This effective path length, coupled with the observed column density of CO and an assumed H_2:CO ratio, allows an estimate of the absolute number density of the cloud. Additionally, when transitions of both ortho- and para-H_3^+ are observed, the observed ortho-to-para ratio can be used to estimate the temperature of the cloud. Unlike in neutral species, the spin modifications in ionic species are thermalized quickly because of rapid Langevin reactions with H_2 (McCall et al. 1998b).

In this work we report the results of a small survey of young stellar objects embedded in dense molecular clouds. H_3^+ was detected in six of the clouds (toward AFGL 2136, W33A, Mon R2 IRS 3, AFGL 961E, AFGL 2591, and AFGL 490) but was not detected in nine others (toward Orion BN, NGC 2024 IRS 2, Mon R2 IRS 2, AFGL 989, Elias 29, M17 IRS 1, W3 IRS 5, S140 IRS 1, and LkHα 101). In two of the clouds that showed H_3^+ absorption (Mon R2 IRS 3 and AFGL 961E), the CO column density had not been reported, so the first overtone of CO was observed.

2. OBSERVATIONS AND DATA REDUCTION

A summary of the observations is provided as Table 1. This table incorporates the initial observations of H_3^+ in 1996 as reported earlier (Geballe & Oka 1996). The $R(1, 0)$ and $R(1, 1)^+$ ortho-para doublet of H_3^+ near 3.67 μm was studied at the 3.8 m United Kingdom Infrared Telescope (UKIRT) on Mauna Kea with the facility spectrometer CGS4 (Mountain et al. 1990), using its echelle at a resolution of 15 km s^{-1}. The UKIRT observations were performed on UT 1996 April 29, 1996 July 15, 1997 February 12-15, and 1997 July 11. The $R(1, 1)^-$ line of para-H_3^+ near 3.71 μm was studied at the 4.0 m Mayall Telescope on

[1] Present address: Gemini Observatory, 670 North A'ohoku Place, Hilo, HI 96720.
[2] Operated by the Association of Universities for Research in Astronomy, Inc. under cooperative agreement with the National Science Foundation.

TABLE 1

LOG OF OBSERVATIONS

Object	UT Date (yy mm dd)	Telescope	Instrument	Molecule	λ (μm)	Integration Time (minute)	Standard
AFGL 2136	960429[a]	UKIRT	CGS4	H_3^+	3.668	5	BS 6378
	960715[a]	UKIRT	CGS4	H_3^+	3.668	7	BS 6378
	970918	Mayall	Phoenix	H_3^+	3.715	78	BS 7001
W33A.....	960429[a]	UKIRT	CGS4	H_3^+	3.668	7	BS 6378
	960715[a]	UKIRT	CGS4	H_3^+	3.668	14	BS 6378
	970711	UKIRT	CGS4	H_3^+	3.668	33	BS 6378
Mon R2 IRS 3	970213	UKIRT	CGS4	H_3^+	3.668	10	BS 2421
	970214	UKIRT	CGS4	H_3^+	3.668	13	BS 1713
	970215	UKIRT	CGS4	H_3^+	3.668	13	BS 1713
	980102	IRTF	CSHELL	CO	2.343	60	BS 3982
	980103	IRTF	CSHELL	CO	2.337	60	BS 3982
AFGL 961E	970212	UKIRT	CGS4	H_3^+	3.668	16	BS 2421
	970213	UKIRT	CGS4	H_3^+	3.668	44	BS 2421
	970214	UKIRT	CGS4	H_3^+	3.668	36	BS 2421
	980102	IRTF	CSHELL	CO	2.343	50	BS 3982
	980103	IRTF	CSHELL	CO	2.337	70	BS 3982
AFGL 2591	970711	UKIRT	CGS4	H_3^+	3.668	6	BS 7924
	970918	Mayall	Phoenix	H_3^+	3.715	23	BS 7001
AFGL 490	970212	UKIRT	CGS4	H_3^+	3.668	16	BS 1040
	970214	UKIRT	CGS4	H_3^+	3.668	13	BS 0936
	970215	UKIRT	CGS4	H_3^+	3.668	13	BS 0936
Orion BN	970212	UKIRT	CGS4	H_3^+	3.668	12	BS 1899
	970215	UKIRT	CGS4	H_3^+	3.668	5	BS 1713
NGC 2024 IRS 2.....	970212	UKIRT	CGS4	H_3^+	3.668	7	BS 2421
	970213	UKIRT	CGS4	H_3^+	3.668	12	BS 1713
	970215	UKIRT	CGS4	H_3^+	3.668	10	BS 1713
Mon R2 IRS 2	970212	UKIRT	CGS4	H_3^+	3.668	11	BS 2421
	970213	UKIRT	CGS4	H_3^+	3.668	10	BS 1713
	970214	UKIRT	CGS4	H_3^+	3.668	16	BS 1790
AFGL 989	970212	UKIRT	CGS4	H_3^+	3.668	9	BS 2421
	970215	UKIRT	CGS4	H_3^+	3.668	7	BS 2421
Elias 29.....	970711	UKIRT	CGS4	H_3^+	3.668	16	BS 5953
M17 IRS 1	970711	UKIRT	CGS4	H_3^+	3.668	19	BS 7340
W3 IRS 5	970917	Mayall	Phoenix	H_3^+	3.715	54	BS 2491
S140 IRS 1.....	970918	Mayall	Phoenix	H_3^+	3.715	57	BS 1713
LkHα 101	970918	Mayall	Phoenix	H_3^+	3.715	18	BS 1713

[a] First reported by Geballe & Oka 1996.

Kitt Peak, using the echelle spectrometer Phoenix (Hinkle et al. 1998), which afforded a resolution of 9 km s^{-1}. The Kitt Peak observations were made on UT 1997 September 17–18. Finally, the $R(0)$–$R(5)$ lines of the first overtone of ^{12}CO near 2.34 μm were studied at the 3.0 m NASA Infrared Telescope Facility (IRTF) on Mauna Kea, using the facility spectrometer CSHELL (Tokunaga, Toomey, & Carr 1990), with a nominal resolution of 15 km s^{-1}. The CO observations were made on UT 1998 January 2–3. The spectra obtained with CGS4 and CSHELL were sampled every one-third resolution element, and those obtained with Phoenix were sampled every 0.18 resolution element.

Standard stars were observed as a part of each observation in order to correct for telluric absorptions. The standard stars used for each source are listed in Table 1. These stars are expected to be featureless in the wavelength regions observed.

Each object (or standard star) was observed alternately at two different beam positions. Each set of exposures was then subtracted in order to remove sky background. The subtracted exposures were then flat-fielded, and bad pixel masks were applied. One-dimensional spectra were then extracted from the resultant images. All extracted spectra for each object (or standard) were then shifted in wavelength when necessary to bring features into coincidence, and then they were summed. The summed spectrum for each object was then divided by a summed spectrum of a standard star, which had been shifted in wavelength and adjusted using Beer's law in order to effect optimum cancellation of telluric absorption lines. Residual interference fringes in the ratio of these spectra were then removed from the resultant spectra using Fourier-transform techniques, and finally the reduced spectrum was wavelength calibrated based on the telluric lines originally present in the spectrum. The wavelength calibration is estimated to be accurate to ± 3 km s^{-1} for the CGS4 and CSHELL spectra and ± 2 km s^{-1} for the Phoenix spectra. A more detailed description of the data reduction technique and the software tools developed for processing these data will be given elsewhere (McCall 1999).

The lines observed are relatively clear of strong telluric absorption lines, with the exception of the $R(1, 1)^+$ line of H_3^+ (with rest wavelength 3.6681 μm), which is quite close to a strong telluric absorption of methane centered at 3.6675 μm. When Doppler shifts are unfavorable, the $R(1, 1)^+$ line can be affected by this methane feature, resulting in rela-

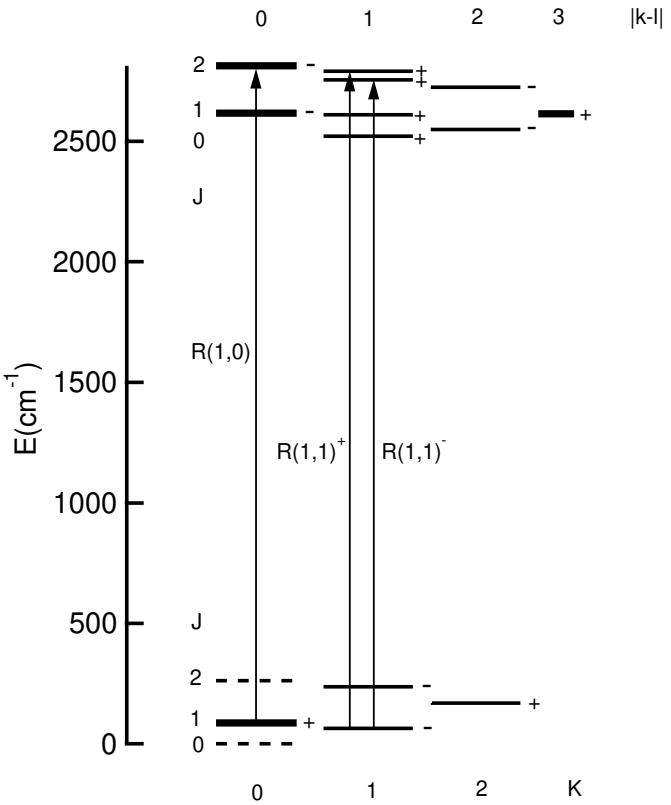

FIG. 1.—Energy-level diagram for the ground state (*below*) and v_2 state (*above*) of H_3^+. The three transitions studied in this work are depicted with vertical arrows. Heavy lines refer to ortho-H_3^+ levels, thin lines refer to para-H_3^+ levels, and dashed lines indicate levels forbidden by the Pauli principle. The plus and minus signs beside the levels indicate the parities of the levels, while the plus and minus signs as superscripts to $R(1, 1)$ simply give the ordering of the levels. In the upper state, the quantum number K is replaced by the quantity $|k - l|$, where l is the quantum number for vibrational angular momentum ($l = \pm 1$ for the v_2 state).

tively large systematic uncertainties in the parameters derived in these cases. Additionally, there are two telluric lines of HDO that lie slightly longer in wavelength than the methane feature. These lines preclude the measurement of the $R(1, 0)$ and $R(1, 1)^+$ lines at Kitt Peak in the summer months, when substantial quantities of water vapor are present.

The H_3^+ rotation-vibration transitions studied are members of the fundamental band of the v_2 degenerate bending mode. An energy-level diagram for the ground state and the v_2 state of H_3^+ is shown in Figure 1, which also shows the three transitions observed. The energy levels of H_3^+ in the vibrational ground state can be described in terms of the quantum numbers I (total nuclear spin), J (rotational angular momentum), and K (projection of the rotational angular momentum along the symmetry axis). The $R(1, 1)^+$ and $R(1, 1)^-$ transitions arise from the lowest allowed level of H_3^+, the $(J, K) = (1, 1)$ level, which has the para ($I = 1/2$) spin modification. The $R(1, 0)$ transition arises from the second lowest level, the $(J, K) = (1, 0)$ level, which has the ortho ($I = 3/2$) spin modification and lies 32.87 K higher. The next higher level, $(J, K) = (2, 2)$, lies 151 K above the (1, 1) level and is therefore expected to have negligible population at the low temperatures of molecular clouds. For more details on the spectroscopic notation, see Oka & Jagod (1993).

3. RESULTS

3.1. H_3^+ *Detections*

The parameters of the observed H_3^+ lines are listed in Table 2. In the case of the $R(1, 1)^-$ line, the equivalent widths W_λ were derived from Gaussian fits to the observed features. In the case of the $R(1, 1)^+$-$R(1, 0)$ doublet, the W_λ were derived from fits to two Gaussians. In the latter fit, all parameters were left free to vary, except in some cases the FWHM was constrained in order to obtain a reasonable fit. The $\sigma(W_\lambda)$ listed in Table 2 is the 1 σ statistical uncertainty, which was calculated from the standard deviation of a straight-line fit to the residuals of the Gaussian fits and the square root of the number of pixels contributing to the feature. The column density for the lower level of each transition, $N_{\rm level}$, was calculated from the standard formula for an optically thin line, $W_\lambda = (8\pi^3\lambda/3hc)N_{\rm level}|\mu|^2$, where $|\mu|^2$ is the square of the transition dipole moment, provided to us by J. K. G. Watson (1992, private communication). Also listed are the corresponding uncertainties in the equivalent width and column density, the observed velocity $v_{\rm obs}$, the

TABLE 2

H_3^+ LINE PARAMETERS[a]

Object	Line	λ (Å)	W_λ (Å)	$\sigma(W_\lambda)$ (Å)	$\lvert\mu\rvert^2$ (D^2)	$N_{\rm level}(H_3^+)$ (10^{14} cm^{-2})	$\sigma(N)$ (10^{14} cm^{-2})	$v_{\rm obs}$ (km s^{-1})	$v_{\rm LSR}$ (km s^{-1})	FWHM (km s^{-1})
AFGL 2136	$R(1, 1)^+$	36680.84	0.049	0.009	0.0158	2.0	0.38	15.8	21.5	21.8
	$R(1, 0)$	36685.16	0.075	0.009	0.0259	1.9	0.23	18.9	24.6	21.9
	$R(1, 1)^-$	37154.78	0.041	0.003	0.0140	1.9	0.14	36.7	21.9	11.2
W33A	$R(1, 1)$	36680.84	0.069	0.019	0.0158	2.9	0.79	30.8	34.3	20[b]
	$R(1, 0)^+$	36685.16	0.091	0.019	0.0259	2.3	0.48	31.0	34.5	20[b]
Mon R2 IRS 3.....	$R(1, 1)^+$	36680.84	0.020	0.006	0.0158	0.83	0.26	47.1	7.6	20[b]
	$R(1, 0)$	36685.16	0.023	0.006	0.0259	0.58	0.16	50.9	11.4	20[b]
AFGL 961E.....	$R(1, 1)^+$	36680.84	0.028	0.008	0.0158	1.2	0.35	47.5	10.2	14.8
	$R(1, 0)$	36685.16	0.024	0.008	0.0259	0.60	0.21	46.7	9.4	14.4
AFGL 490	$R(1, 1)^+$	36680.84	0.016	0.010	0.0158	0.66	0.39	10.3	−11.4	19.9
	$R(1, 0)$	36685.16	0.015	0.009	0.0259	0.37	0.22	12.4	−9.4	17.2
AFGL 2591	$R(1, 1)^+$	36680.84	0.051	0.004	0.0158	2.1	0.18	−27.9	−1.2	20[b]
	$R(1, 0)$	36685.16	0.039	0.004	0.0259	0.98	0.11	−35.4	−8.8	20[b]
	$R(1, 1)^-$	37154.78	0.025	0.002	0.0140	1.2	0.07	−7.6	1.2	14.7

[a] Statistical uncertainties (1 σ) are listed. Systematic errors are difficult to estimate and may be larger.
[b] For these objects the FWHM was constrained to the listed value in order to effect a reasonable fit.

TABLE 3

COMPARISON OF v_{LSR} OF H_3^+ AND CO

Object	H_3^+ v_{LSR}[a] (km s^{-1})	Infrared CO v_{LSR} (km s^{-1})	Millimeter CO v_{LSR} (km s^{-1})
AFGL 2136	22.7	26.5 ± 2.8[b]	27.2[c]
W33A	34.4	32.6 ± 1.7[b]	36[d]
Mon R2 IRS 3.....	9.5	9.7[e]	10.7[f]
AFGL 961E.....	9.8	12.4[e]	12.5[g]
AFGL 2591[h]	−2.9	−10.7 ± 0.4[b]	−6[i]
AFGL 490	−10.4	−13.5[i]	−13.5[j]

[a] Average v_{LSR} of observed lines. The estimated uncertainty is ±3 km s^{-1}.
[b] Mitchell et al. 1990.
[c] Dinger et al. 1979.
[d] Goldsmith & Mao 1983.
[e] This work.
[f] Maddalena et al. 1986.
[g] Schneider et al. 1998.
[h] The H_3^+ v_{LSR} for AFGL 2591 is uncertain and may be bluer owing to telluric interference, as discussed in the text.
[i] Bally & Lada 1983.
[j] Mitchell et al. 1995.

derived velocity with respect to the local standard of rest v_{LSR}, and the FWHM.

Table 3 compares the LSR velocities derived from our H_3^+ measurements with those derived from infrared and millimeter CO measurements. The agreement between the H_3^+ and CO velocities, along with the correct observed separations of the $R(1, 1)^+$-$R(1, 0)$ doublet, is strong evidence of the reality of the H_3^+ features.

As was previously reported (Geballe & Oka 1996), the lines of sight toward AFGL 2136 and W33A were observed at 3.67 μm at UKIRT on the nights of UT 1996 April 29 and 1996 July 15. The data from these observations have recently been reprocessed, and the H_3^+ ortho-para doublet is clearly visible in both data sets, taken 77 days apart (Fig. 2). The H_3^+ lines show the expected change in observed wavelength due to the Earth's orbital motion over this time, providing strong evidence that the individual detections are genuine.

Figure 3 shows the reduced spectra of the H_3^+ doublet in the lines of sight toward Mon R2 IRS 3, AFGL 961E, and AFGL 490. The case of AFGL 490 might be considered a marginal detection because of the low signal-to-noise ratio, but the correct separation of the observed doublet suggests that the detection is probably secure. The equivalent widths of the H_3^+ absorptions in each of these objects are less than half of those toward W33A and AFGL 2136.

Figure 4 shows the reduced spectra of AFGL 2136 and AFGL 2591. In both cases, the $R(1, 1)^+$-$R(1, 0)$ doublet was observed using CGS4 at UKIRT (the spectrum of AFGL 2136 shown is from 1996 July 15) and the $R(1, 1)^-$ line was observed using Phoenix at Kitt Peak. In the case of AFGL 2136, both spectra are of good quality and the column densities of para-H_3^+ derived from the $R(1, 1)^+$ and $R(1, 1)^-$ lines are in good agreement. In the case of AFGL 2591, the doublet in the UKIRT spectrum is unresolved owing to an unfavorable Doppler shift into the region of the telluric lines and the short integration time. However, coupled with the observation of the $R(1, 1)^-$ line at Kitt Peak, the detection appears secure. The fact that the $R(1, 1)^-$ line was also unfavorably Doppler-shifted into the shoulder of a telluric line at 3.7152 μm may have effectively redshifted the center of the observed line by partially obscuring the blue side of

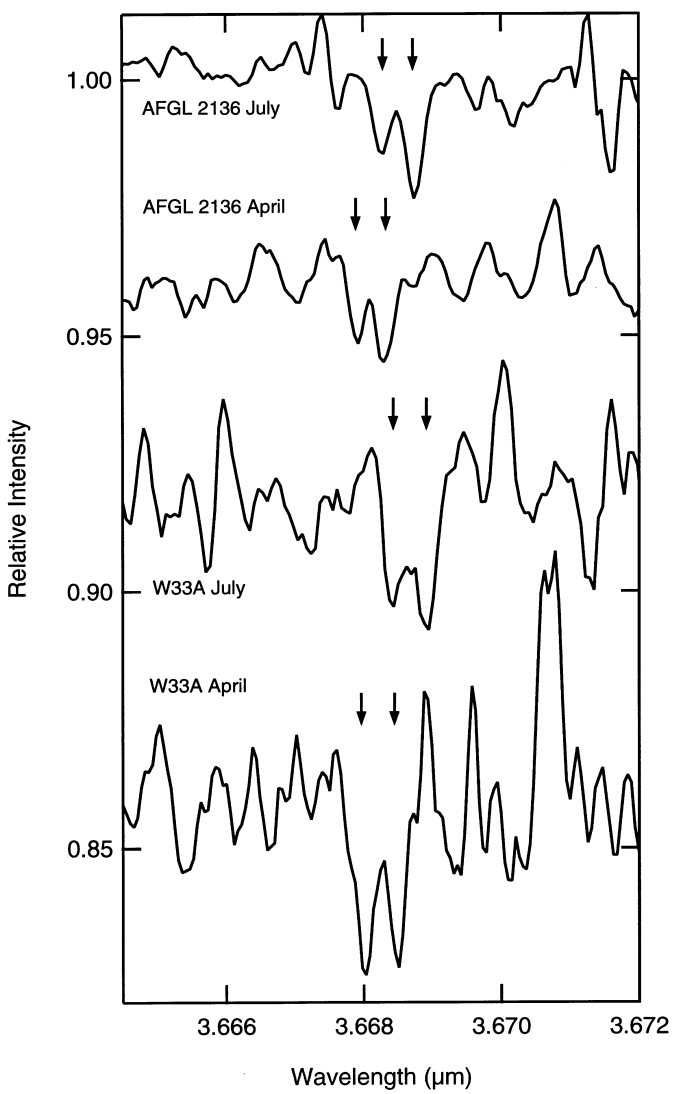

FIG. 2.—Spectra of the $R(1, 1)^+$-$R(1, 0)$ doublet of H_3^+ toward AFGL 2136 and W33A, obtained with UKIRT in 1996 July and April. The arrows indicate the H_3^+ lines. In Figs. 2–6 the lower traces are shifted downward from unity, and the spectra have been smoothed to reduce pixel-to-pixel variations for clarity.

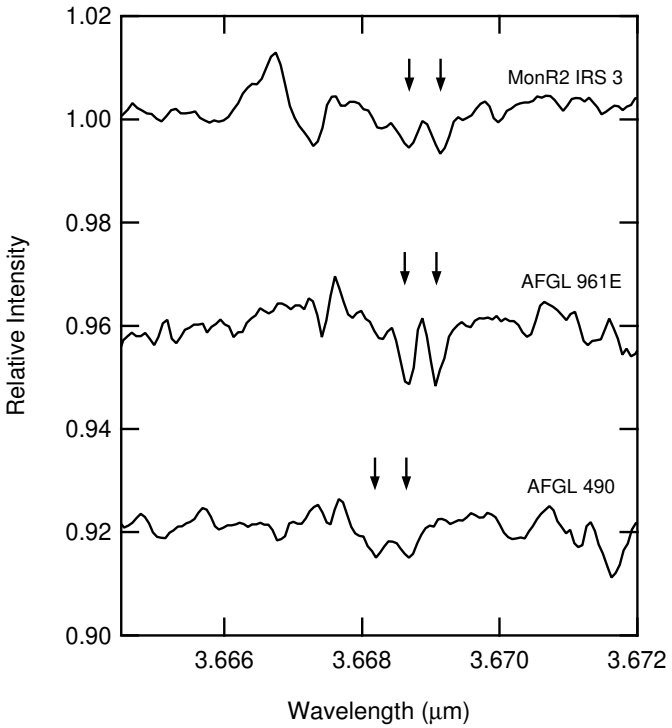

FIG. 3.—Spectra of the $R(1, 1)^+$-$R(1, 0)$ doublet of H_3^+ toward Mon R2 IRS 3, AFGL 961E, and AFGL 490, obtained with UKIRT. The arrows indicate the H_3^+ lines.

TABLE 4

H_3^+ NONDETECTIONS[a]

Object	Line	$\sigma(W_\lambda)$ (Å)	$\sigma(N_{level})$ (10^{14} cm^{-2})
Orion BN	$R(1, 1)^+$	0.012	0.51
	$R(1, 0)$	0.012	0.31
NGC 2024 IRS 2.....	$R(1, 1)^+$	0.0071	0.29
	$R(1, 0)$	0.0071	0.18
Mon R2 IRS 2	$R(1, 1)^+$	0.010	0.42
	$R(1, 0)$	0.010	0.26
AFGL 989	$R(1, 1)^+$	0.0057	0.24
	$R(1, 0)$	0.0057	0.15
Elias 29.....	$R(1, 1)^+$	0.012	0.50
	$R(1, 0)$	0.012	0.31
M17 IRS 1	$R(1, 1)^+$	0.054	2.2
	$R(1, 0)$	0.054	1.4
W3 IRS 5	$R(1, 1)^-$	0.0038	0.18
S140 IRS 1.....	$R(1, 1)^-$	0.0020	0.091
LkHα 101	$R(1, 1)^-$	0.0049	0.23

[a] The firm upper limits for these nondetections should be considered 3 σ. Upper limits have been derived using an assumed FWHM of 20 km s^{-1} for all UKIRT spectra and 15 km s^{-1} for KPNO spectra (the last three entries).

the line, so that the true v_{LSR} may be more negative than our analysis reveals.

3.2. H_3^+ *Upper Limits*

Table 4 summarizes our nondetections of H_3^+ in the dense clouds along the lines of sight to Orion BN, NGC 2024 IRS 2, Mon R2 IRS 2, AFGL 989, Elias 29, M17 IRS 1, W3 IRS 5, S140 IRS 1, and LkHα 101. The 1 σ deviations of the baseline, computed for an assumed line width of 20 km s^{-1} for the first six objects (observed with CGS4) and 15 km s^{-1} for the last three objects (observed with Phoenix), are listed in the table. The firm upper limits for these nondetections should be considered 3 σ. The CGS4 spectra are shown in Figure 5, and the Phoenix spectra are shown in Figure 6. In the spectra of Mon R2 IRS 2 and NGC 2024 IRS 2, the $R(1, 1)^+$-$R(1, 0)$ doublets appear to be present near the expected positions, but the signal-to-noise ratios are too low to consider these as firm detections. We recently learned that Kulesa & Black (1999) detected H_3^+ with rea-

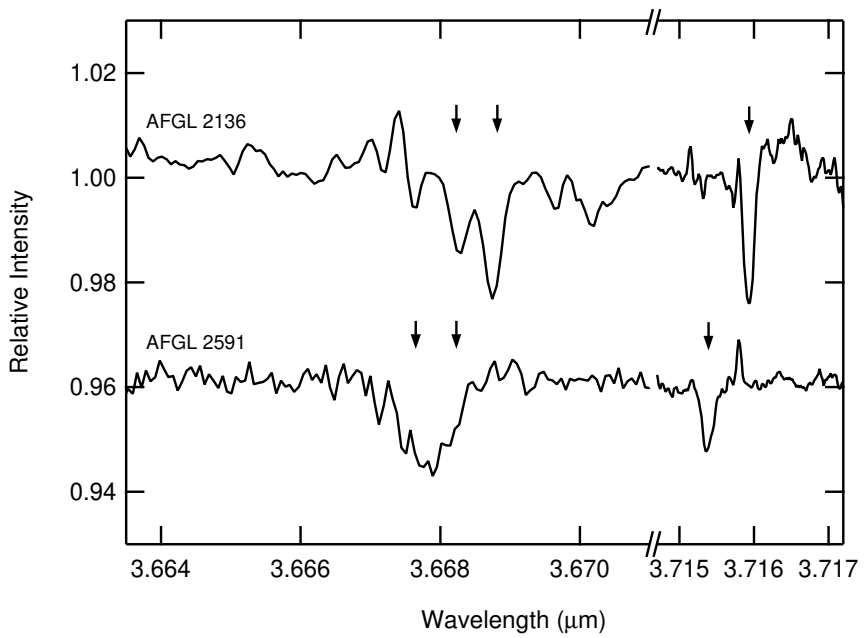

FIG. 4.—Spectra of the $R(1, 1)^+$-$R(1, 0)$ doublet of H_3^+ obtained with UKIRT (*left*) and the $R(1, 1)^-$ line of H_3^+ obtained at Kitt Peak (*right*), toward AFGL 2136 (1996 July 15) and AFGL 2591. The arrows indicate the H_3^+ lines.

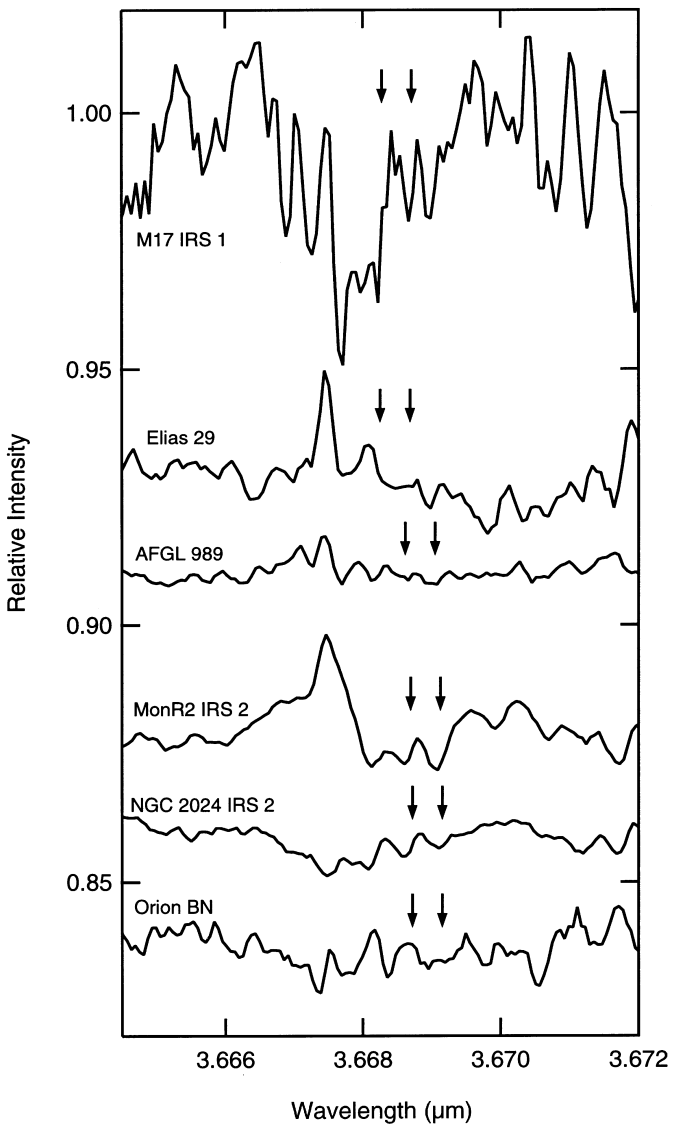

FIG. 5.—Nondetections of the $R(1, 1)^+$-$R(1, 0)$ doublet of H_3^+ toward six dense cloud sources from UKIRT data. The arrows indicate the expected positions of the H_3^+ lines.

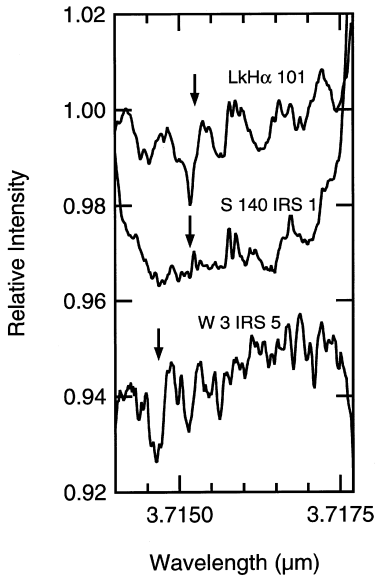

FIG. 6.—Nondetections of the $R(1, 1)^-$ line of H_3^+ toward three dense cloud sources from Kitt Peak. The arrows indicate the expected positions of the H_3^+ line.

sonable signal-to-noise ratio in NGC 2024 IRS 2 at Kitt Peak using long integrations.

3.3. CO *Detections*

Table 5 summarizes our observations of CO toward AFGL 961E and Mon R2 IRS 3. In both cases the first six lines of the *R*-branch were observed with good signal-to-noise ratios. The observed spectra are shown in Figure 7. The transition dipole moments were calculated from *f*-values obtained from the ab initio calculations of Huré & Roueff (1996). The nonlinearity of the absorption was taken into account in calculating the column densities. Figure 8 shows the Boltzmann plots for these two sources. For Mon R2 IRS 3, a straight-line fit yields an excitation temperature of 80 K. For AFGL 961E, the fit yields $T_{ex} = 6$ K and $J = 1$–5 yields $T_{ex} = 39$ K. The rotational distribution of

TABLE 5

CO LINE PARAMETERS.[a]

Object	Line	λ (Å)	W_λ (Å)	$\sigma(W_\lambda)$ (Å)	$\lvert\mu\rvert^2$ (10^{-5} D^2)	N_{level} (10^{17} cm^{-2})	$\sigma(N)$ (10^{17} cm^{-2})	v_{obs} (km s^{-1})	v_{LSR} (km s^{-1})	FWHM (km s^{-1})
AFGL 961E.....	*R*(0)	23453.05	0.220	0.005	4.28	5.37	0.20	29.5	11.9	12.1
	R(1)	23432.69	0.176	0.004	2.87	6.23	0.15	29.7	12.1	10.7
	R(2)	23412.75	0.249	0.005	2.60	9.83	0.33	30.6	13.0	12.8
	R(3)	23393.23	0.241	0.010	2.49	10.1	0.51	29.4	11.3	14.4
	R(4)	23374.13	0.146	0.006	2.43	6.84	0.53	28.7	10.5	11.5
	R(5)	23355.44	0.102	0.008	2.40	4.62	0.36	33.8	15.7	11.5
Mon R2 IRS 3.....	*R*(0)	23453.05	0.249	0.007	4.28	7.69	0.23	28.6	6.0	14.6
	R(1)	23432.69	0.300	0.005	2.87	14.8	0.46	32.6	10.0	13.0
	R(2)	23412.75	0.423	0.006	2.60	28.9	0.90	33.7	11.1	15.2
	R(3)	23393.23	0.429	0.006	2.49	30.8	1.07	33.8	10.8	14.9
	R(4)	23374.13	0.401	0.005	2.43	28.0	0.82	31.4	8.3	15.1
	R(5)	23355.44	0.385	0.007	2.40	27.0	0.97	35.1	12.1	15.7

[a] Statistical uncertainties (1 σ) are listed. Systematic errors due to incomplete cancellation of telluric CO lines are difficult to estimate and probably larger.

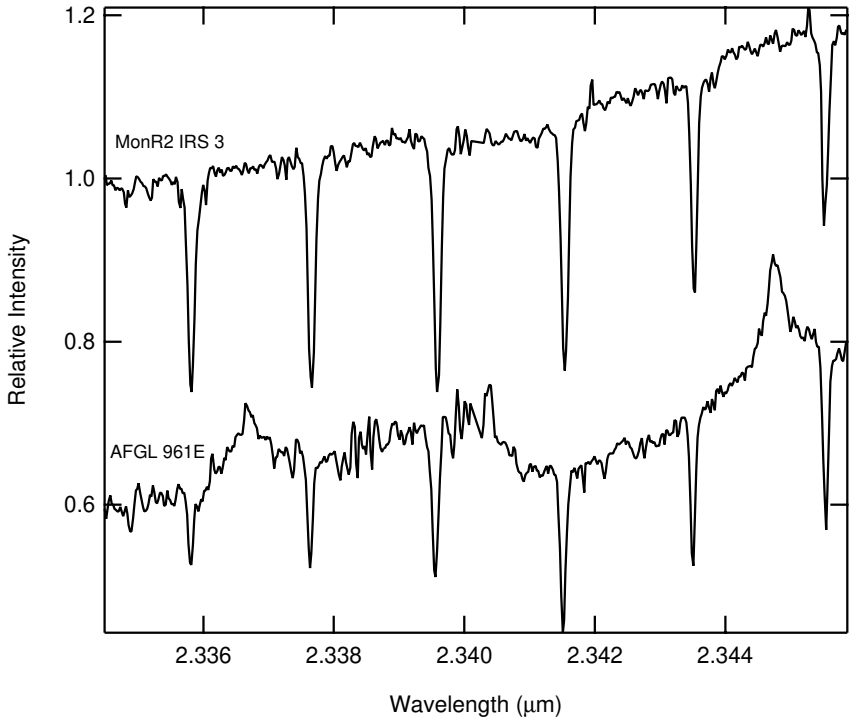

FIG. 7.—^{12}CO first overtone spectra of Mon R2 IRS 3 and AFGL 961E obtained at IRTF. The emission features in the AFGL 961E spectrum are Pfund series lines from high n (30, 31, and 32). The spectrum of AFGL 961E has been shifted downward for clarity.

CO in molecular clouds has been discussed by Mitchell et al. (1990). We estimate total CO column densities of 1.9×10^{19} cm^{-2} for Mon R2 IRS 3 and 0.5×10^{19} cm^{-2} for AFGL 961E.

4. DISCUSSION

4.1. H_3^+ *Chemistry in Molecular Clouds*

4.1.1. H_3^+ *Formation*

In the interstellar medium, as in the laboratory, H_3^+ is formed in a two-step reaction sequence: the ionization of H_2 to form H_2^+, followed by the Langevin reaction $H_2^+ + H_2 \rightarrow H_3^+ + H$. Since the Langevin reaction is quite fast (rate constant $k \sim 2 \times 10^{-9}$ cm^3 s^{-1}; Bowers, Elleman, & King 1969), the rate of formation of H_3^+ is completely determined by the rate of H_2 ionization.

The process generally assumed to dominate the ionization of H_2 is bombardment by cosmic-ray protons with energies near 100 MeV (Herbst & Klemperer 1973). At these energies, protons can travel through an H_2 column of $\sim 10^{24}$ cm^{-2}, which is more than the column densities of typical dense clouds. As a result, the rate of cosmic-ray ionization should be relatively constant and has been estimated (Herbst & Klemperer 1973) to be $\zeta \sim 10^{-17}$ s^{-1}. The order of magnitude of this result has been confirmed by observations of HCO^+ and DCO^+ (Plume et al. 1998). Recently used values of ζ average around 3×10^{-17} s^{-1} (van Dishoeck & Black 1986; Lee, Bettens, & Herbst 1996), so we adopt this value.

Ionization of H_2 by ultraviolet photons should not be a significant source of H_2^+ in dense clouds because photons with sufficient energy (15.4 eV) will not penetrate the clouds

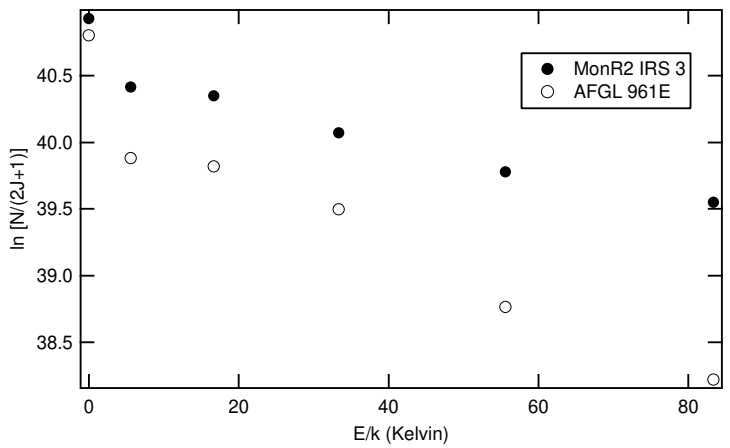

FIG. 8.—Boltzmann plots for the ^{12}CO overtone observations of Mon R2 IRS 3 and AFGL 961E

even if they escape the H II regions around their sources. The ionization of H_2 by X-rays has also been suggested as an efficient process leading to H_3^+ formation (Draine & Woods 1990; Black 1998). However, this mechanism could operate only in unusual environments near strong X-ray sources, such as active galactic nuclei, and is probably not important in most dense clouds in our Galaxy.

Thus, for the remainder of the discussion in this paper, we adopt the usual assumption that H_2^+ production is dominated by cosmic-ray ionization and therefore that the H_3^+ production rate is $\zeta n(H_2)$, where $\zeta \sim 3 \times 10^{-17}$ s^{-1}.

4.1.2. H_3^+ *Destruction*

The destruction of H_3^+ in dense clouds is dominated by chemical reactions that lead (after subsequent reactions) to more complicated molecules. Reactions of H_3^+ with hydrogen species (H_2 or H) do not cause a net loss of H_3^+, and the reaction with He (the next most abundant element) to form HeH^+ is endothermic by 2.6 eV and cannot occur at the low temperatures of dense clouds.

The next most abundant elements are C and O, and we expect that the destruction of H_3^+ should be dominated by species containing these elements. In dense clouds, over 99% of gas-phase carbon atoms are in the form of CO, and of the O atoms that are not in CO, the majority exist as free atoms according to the extensive chemical model calculation by Lee et al. (1996). Since the reaction rate of H_3^+ with O is slower than that with CO, the destruction of H_3^+ is dominated by reaction with CO.

Table 6 shows the eight species that most efficiently destroy H_3^+ in dense clouds. In this table we have listed, for each species, the maximum and minimum abundances in steady state from the "new standard model" of Lee et al. (1996) for hydrogen densities from 10^3–10^5 cm^{-3} and temperatures from 10–50 K. Also listed are the measured rate constants with H_3^+ and the minimum and maximum expected rates of H_3^+ destruction. The electron is one noteworthy entry—electron recombination, which in diffuse clouds is the primary destruction path of H_3^+, is seen not to play a major role in the dense cloud environment because of the lower electron abundance.

In the following discussion we will consider only H_3^+ destruction by CO for reasons of simplicity. Clearly a rigorous quantitative model must take into account the contribution ($\sim$20%–30% of the total destruction) of atomic oxygen. However, since the cosmic-ray ionization rate ζ is uncertain to a factor on the order of a few, the neglect of oxygen in this model is not a serious omission. In our discussions here we take the rate of H_3^+ destruction to be given by the simple expression $k_{CO}\, n(CO) n(H_3^+)$.

4.1.3. H_3^+ *Abundance*

To estimate the abundance of H_3^+ in dense clouds, we make the assumption of a steady state and equate the rates of formation and destruction. From §§ 4.1.1 and 4.1.2, this gives $\zeta n(H_2) = k_{CO}\, n(CO) n(H_3^+)$. This equation can be rearranged to yield the number density of H_3^+:

$$n(H_3^+) = \frac{\zeta}{k_{CO}} \frac{n(H_2)}{n(CO)} . \quad (1)$$

In order to obtain a numerical estimate, we substitute $\zeta \sim 3 \times 10^{-17}$ s^{-1}, $k_{CO} = 2 \times 10^{-9}$ cm^3 s^{-1}, and $n(CO)/n(H_2) \sim 1.5 \times 10^{-4}$ (Lee et al. 1996). This yields a value of $n(H_3^+) \sim 1 \times 10^{-4}$ cm^{-3}. As mentioned earlier, H_3^+ (unlike most molecules) has a constant number density in molecular clouds independent of total H_2 number density; because of this, measurements of H_3^+ column density can be of distinct value in determining cloud parameters.

4.1.4. *Ortho-to-Para Ratio*

The ratio of ortho- to para-H_3^+ in dense clouds is expected to reflect the kinetic temperature of the background (H_2) gas. This is because ortho- and para-H_3^+ are not linked by any radiative transitions but are linked by ion-neutral reactions with H_2 that proceed at the Langevin rate ($k \sim 2 \times 10^{-9}$ cm^3 s^{-1}). The proton hop reaction

$$H_3^+ + \tilde{H}_2 \rightarrow H_2 + \tilde{H}_2 H^+ \quad (2)$$

and the proton exchange reaction

$$H_3^+ + \tilde{H}_2 \rightarrow H_2 \tilde{H}^+ + H\tilde{H} \quad (3)$$

scramble protons between H_2 and H_3^+ and thereby thermalize the spin temperature of H_3^+ to the kinetic temperature of H_2 (Uy, Cordonnier, & Oka 1997). In the above reactions, the tildes indicate the protons from the reactant H_2.

4.2. *Estimates of Cloud Parameters*

Because the number density of H_3^+ is independent of the total H_2 number density, the observed column density of H_3^+ directly yields an estimate of the effective column length of absorption. This corresponds physically to the length of the portion of the cloud that lies along the line of sight to

TABLE 6

SPECIES IMPORTANT IN THE DESTRUCTION OF H_3^+

Species	Minimum Abundance $[n/n(H_2)]$	Maximum Abundance $[n/n(H_2)]$	Rate Constant (cm^{3}s^{-1})	Minimum Rate $[s^{-1}/n(H_2)]$	Maximum Rate $[s^{-1}/n(H_2)]$
CO	1.45 (−4)	1.46 (−4)	1.8 (−9)[a]	2.6 (−13)	2.6 (−13)
O	8.64 (−5)	1.51 (−4)	8.0 (−10)[b]	6.9 (−14)	1.2 (−13)
e^-	1.89 (−8)	2.31 (−7)	1.8 (−7)[c]	3.4 (−15)	4.2 (−14)
N_2	5.86 (−6)	1.92 (−5)	1.8 (−9)[a]	1.1 (−14)	3.5 (−14)
O_2	2.68 (−5)	5.92 (−5)	2.7 (−10)[d]	7.2 (−15)	1.6 (−14)
H_2O	3.59 (−7)	2.32 (−6)	5.9 (−9)[a]	2.1 (−15)	1.4 (−14)
N	4.34 (−6)	3.08 (−5)	4.5 (−10)[e]	2.0 (−15)	1.4 (−14)
CO_2	1.41 (−7)	9.45 (−7)	2.0 (−9)[a]	2.8 (−16)	1.9 (−15)

[a] Anicich & Huntress 1986.
[b] Fehsenfeld 1976.
[c] Amano 1988; Sundström et al. 1994 give a temperature dependent rate constant of $4.6 \times 10^{-6}\, T^{-0.65}$ cm^3 s^{-1}.
[d] Adams & Smith 1984.
[e] Scott et al. 1997.

TABLE 7

ESTIMATED CLOUD PARAMETERS

Object	$N_o(H_3^+)$ (10^{14} cm^{-2})	$N_p(H_3^+)$[a] (10^{14} cm^{-2})	$N_{tot}(H_3^+)$ (10^{14} cm^{-2})	ζL (cm s^{-1})	L (parsec)	$\tau_{9.7}$[b]	N_H[c] (10^{22} cm^{-2})	N(CO) (10^{19} cm^{-2})	$N(H_2)$[d] (10^{22} cm^{-2})	$\langle n(H_2)\rangle$ (10^4 cm^{-3})	T (K)
AFGL 2136	1.9	1.9	3.8	110	1.3	5.07	18	3.2[f]	22	6	47
W33A	2.3	2.9	5.2	150	1.7	7.84	28	3.9[f]	27	5	36
Mon R2 IRS 3.....	0.6	0.8	1.4	41	0.5	2[e]	7	1.9[g]	1.3	9	31
AFGL 961E.....	0.6	1.1	1.7	49	0.6	2.11	7.5	0.5[g]	3.2	2	25
AFGL 490	0.4	0.7	1.1	32	0.4	2.77	9.8	1.1[h]	7.6	6	26
AFGL 2591[i]	1.0	1.2	2.2	64	0.7	4.14	15	1.9[f]	13	6	38

[a] For AFGL 2136 and AFGL 2591, where both the $R(1, 1)^+$ and $R(1, 1)^-$ para-H_3^+ lines were observed, the $R(1, 1)^-$ values have been used because they have a lower $\sigma(N)$.

[b] Silicate optical depths at 9.7 μm from Willner et al. 1982, except as noted.

[c] Hydrogen column derived from $A_V/\tau_{9.7} = 18.6$ (Roche & Aitken 1994) and $N_H/A_V = 1.9 \times 10^{21}$ cm^{-2} mag^{-1} (Bohlin, Savage, & Drake 1978).

[d] Hydrogen column derived from $n(CO)/n(H_2) \sim 1.5 \times 10^{-4}$ from Lee et al. 1996.

[e] Beckwith et al. 1976.

[f] Mitchell et al. 1990.

[g] This work.

[h] Mitchell et al. 1995, assuming $^{12}CO/^{13}CO = 89$.

[i] Estimates for AFGL 2591 have large systematic uncertainties due to the short integration time and telluric interference, as discussed in the text.

the infrared source. We estimate this length from the following approximate relation

$$L \sim \frac{N(H_3^+)}{n(H_3^+)}, \quad (4)$$

where $n(H_3^+)$ has been estimated to be $\sim 1 \times 10^{-4}$ cm^{-3}. The resulting lengths are on the order of a parsec, consistent with the usual dimensions of molecular clouds.

Given the effective column length of a cloud, we estimate the absolute number density of H_2, assuming that the majority of the H_2 along the line of sight is contained in the molecular cloud where the H_3^+ absorption is seen. The column density of H_2 is estimated from the observed column density of CO using $n(CO)/n(H_2) \sim 1.5 \times 10^{-4}$ from the model calculations of Lee et al. (1996). For comparison, in Table 7 we have also estimated N_H from the silicate optical depth as prescribed by Tielens et al. (1991). We note that the estimated values of N_H and $2N(H_2)$ are quite similar, within a factor of a few. Given an estimate of $N(H_2)$, we estimate the mean hydrogen number density

$$\langle n(H_2) \rangle \sim \frac{N(H_2)}{L} \sim \frac{N(H_2)}{N(H_3^+)} n(H_3^+) . \quad (5)$$

Finally, the observed H_3^+ ortho-to-para ratio allows us to estimate the kinetic temperature of the cloud using the standard Boltzmann formula,

$$\frac{N_{ortho}}{N_{para}} = \frac{g_{ortho}}{g_{para}} e^{-\Delta E/kT} = 2e^{-32.87/T}, \quad (6)$$

where the g values are the statistical weights of the ortho- and para-H_3^+ states and ΔE is the energy difference between them.

The estimated column lengths, H_2 number densities, and kinetic temperatures for the sources where H_3^+ has been detected are listed in Table 7. These values pertain only to the portions of the clouds in front of the infrared sources. Note that the derived values of L are inversely proportional to the assumed value of ζ and the values of $\langle n(H_2) \rangle$ are proportional to ζ, so both are uncertain to a factor on the order of a few.

Measurements of H_3^+, along with an assumed H_2:CO ratio, directly provide an accurate value of the quantity ζL but cannot constrain ζ or L independently. Better estimates of either ζ or L, along with improved determinations of the H_2:CO ratio using infrared spectroscopy (e.g., Lacy et al. 1994), will allow more accurate estimates of $\langle n(H_2) \rangle$. As extensive models of molecular clouds (from core to edge) are developed from radio and millimeter observations, it will be of considerable interest to compare these models with the estimates of $\langle n(H_2) \rangle$ from H_3^+ observations.

5. CONCLUSIONS

The fundamental molecular ion H_3^+ has now been detected along many lines of sight in the interstellar medium. In addition to the initial detections in the dense molecular clouds toward AFGL 2136 and W33A, H_3^+ has also been detected toward the dense cloud sources Mon R2 IRS 3, AFGL 961E, AFGL 2591, and AFGL 490 with column densities ~ 1–2×10^{14} cm^{-2}.

The nondetections reported here should not be taken as due to the absence of H_3^+ but rather as due to a lack of sensitivity in the observations. In many cases, the established upper limits to H_3^+ are higher than observed H_3^+ column densities in other sources, so that H_3^+ may be detectable in these clouds using longer integrations or more sensitive spectrometers. In the cases where the upper limits are very low (e.g., S140 IRS 1), it is likely that H_3^+ is still present, but that the absorption path length is too short to permit detection at current levels of sensitivity.

The simplicity of interstellar H_3^+ chemistry enables estimates of the effective path lengths, the hydrogen number densities, and the kinetic temperatures of the gas in these dense clouds. The fact that the resulting estimates are consistent with the canonical values for dense clouds represents an important confirmation of the theory of H_3^+ chemistry in this environment. The observation of H_3^+ in several dense molecular clouds, along with the recent detections of H_3^+ in the diffuse interstellar medium and toward the Galactic center, confirms the expected ubiquity of H_3^+ and demonstrates its promise as a powerful probe of the interstellar medium.

We thank the staffs of the Joint Astronomy Centre, the United Kingdom Infrared Telescope, and the Kitt Peak National Observatory for the support of these measurements. Some of the observations reported here were made during UKIRT Service observing. UKIRT is operated by the Joint Astronomy Centre on behalf of the U.K. Particle Physics and Astronomy Research Council. B. J. McCall is supported by the Fannie and John Hertz Foundation. The University of Chicago portion of this work has been supported by NSF grant PHYS-9722691 and NASA grant NAG5-4070.

REFERENCES

Adams, N. G., & Smith, D. 1984, Chem. Phys. Lett., 105, 604
Amano, T. 1988, ApJ, 329, L121
Anicich, V. G., & Huntress, W. T., Jr., 1986, ApJS, 62, 553
Bally, J., & Lada, C. J. 1983, ApJ, 265, 824
Beckwith, S., Evans, N. J., II, Becklin, E. E., & Neugebauer, G. 1976, ApJ, 208, 390
Black, J. H. 1998, Faraday Discuss., 109, 257
Bohlin, R. C., Savage, B. D., & Drake, J. F. 1978, ApJ, 224, 132
Bowers, M. T., Elleman, D. D., & King, J., Jr. 1969, J. Chem. Phys., 50, 4787
Dinger, A., Dickinson, D. F., Gottlieb, C. A., & Gottlieb, E. W. 1979, PASP, 91, 830
Draine, B. T., & Woods, D. T. 1990, ApJ, 363, 464
Fehsenfeld, F. C. 1976, ApJ, 209, 638
Geballe, T. R., McCall, B. J., Hinkle, K. H., & Oka, T. 1999, ApJ, 510, 251
Geballe, T. R., & Oka, T. 1996, Nature, 384, 334
Goldsmith, P. F., & Mao, X.-J. 1983, ApJ, 265, 791
Herbst, E., & Klemperer, W. 1973, ApJ, 185, 505
Hinkle, K. H., Cuberly, R., Gaughan, N., Heynssens, J., Joyce, R., Ridgway, S. T., Schmitt, P., & Simmons, J. E. 1998, Proc. SPIE, 3354, 810
Huré, J. M., & Roueff, J. M. 1996, A&AS, 117, 561
Kulesa, C., & Black, J. H. 1999, in preparation
Lacy, J. H., Knacke, R., Geballe, T. R., & Tokunaga, A. T. 1994, ApJ, 428, L69
Lee, H.-H., Bettens, R. P. A., & Herbst, E. 1996, A&AS, 119, 111
Maddalena, R. J., Morris, M., Moscowitz, J., & Thaddeus, P. 1986, ApJ, 303, 375
McCall, B. J. 1999, in preparation
McCall, B. J., Geballe, T. R., Hinkle, K. H., & Oka, T. 1998a, Science, 279, 1910
McCall, B. J., Hinkle, K. H., Geballe, T. R., & Oka, T. 1998b, Faraday Discuss., 109, 267
Mitchell, G. F., Lee, S. W., Maillard, J.-P., Matthews, H., Hasegawa, T. I., & Harris, A. I. 1995, ApJ, 438, 794
Mitchell, G. F., Maillard, J.-P., Allen, M., Beer, R., & Belcourt, K. 1990, ApJ, 363, 554
Mountain, C. M., Robertson, D. J., Lee, T. J., & Wade, R. 1990, Proc. SPIE, 1235, 25
Oka, T. 1980, Phys. Rev. Lett., 45, 531
Oka, T., & Jagod, M.-F. 1993, J. Chem. Soc. Faraday Trans., 89, 2147

Plume, R., Bergin, E. A., Williams, J. P., & Myers, P. C. 1998, Faraday Discuss., 109, 47
Roche, P. F., & Aitken, D. K. 1984, MNRAS, 208, 481
Schneider, N., Stutzki, J., Winnewisser, G., & Block, D. 1998, A&A, 335, 1049
Scott, G. B. I., Fairley, D. A., Freeman, C. G., & McEwan, M. J. 1997, Chem. Phys. Lett., 269, 88
Sundström, G., et al. 1994, Science, 263, 785
Tielens, A. G. G. M., Tokunaga, A. T., Geballe, T. R., & Baas, F. 1991, ApJ, 381, 181
Tokunaga, A. T., Toomey, D. W., & Carr, J. S. 1990, Proc. SPIE, 1235, 131
Uy, D., Cordonnier, M., & Oka, T. 1997, Phys. Rev. Lett., 78, 3844
van Dishoeck, E. F., & Black, J. H. 1986, ApJS, 62 109
Watson, W. D. 1973, ApJ, 183, L17
Willner, S. P., et al. 1982, ApJ, 253, 174